Rapid response of Helheim Glacier in Greenland to climate variability over the past century

Andresen et al.

Content:
1. Bathymetry
2. Sediment cores
3. Helheim Glacier margin images
4. Oceanographic data
5. Statistical computations

1. Bathymetry

The bathymetric map of Sermilik Fjord was compiled from 372,000 depth measurements from field surveys conducted by teams from the Geological Survey of Denmark and Greenland (GEUS), Woods Hole Oceanographic Institution (WHOI), Swansea University (SU) and Nansen Environmental Remote Sensing Center (NERSC)[31]. The bathymetry documents a U-shaped fjord with steep side walls and depths of 920 m at the mouth and 600 m at the northern end of the fjord extending approximately in a north-south direction. The width of the fjord ranges from 5 to 12 km. The absence of large sills inside the fjord suggests that icebergs are free to drift out of the fjord without grounding on shallower grounds. This is also supported by a shallow seismic survey revealing mostly stratified sediments with no traces of iceberg scouring on the sea bottom[32].

2. Sediment cores

Sediment coring was performed from a locally chartered vessel "Erik den Røde" using a Rumohr corer, with core liners up to 1.5 m in length and a diameter of 8 cm. This coring device has no core catcher, which ensured collection of undisturbed surface sediments. All cores were immediately stored vertically. Core ER13 was retrieved from 660 m water depth (66°05'50"N, 37°52'54W), core ER07 from 525 m water depth (66°00'59"N, 37°51'07"W) and core ER11 from 600 m water depth (65°55'29"N, 37°50'52"W) and the distance is c. 10 km between cores. The cores were split in two halves, one for sub sampling and one for X-ray radiography.

2.1 X-ray radiography

The split core halves were cut into ca. 30 cm pieces and X-radiographed at the Royal Netherlands Institute for Sea Research. X-ray radiography of the cores shows diamicton facies and sand layers with erosive boundaries (Supplementary Fig. S1). Core ER13 consists of diamicton facies with a diffuse layering. Below 80 cm layers are frequently current laminated/stratified. A marked sand layer from 53.5 cm to 58-60 cm topped by a 2 cm clayey laminated silt layer and with an undulating lower contact, represents a well-defined turbidite. Cores ER07 and ER11 are characterised by massive diamicton facies with abundant pebbles and in core ER07 a very sandy unit, while an upper erosional boundary is evident at 124-135 cm. This unit may also be interpreted as a turbidite. Apart from these there are no indications of additional turbidites in the cores.

ER13

ER07

2
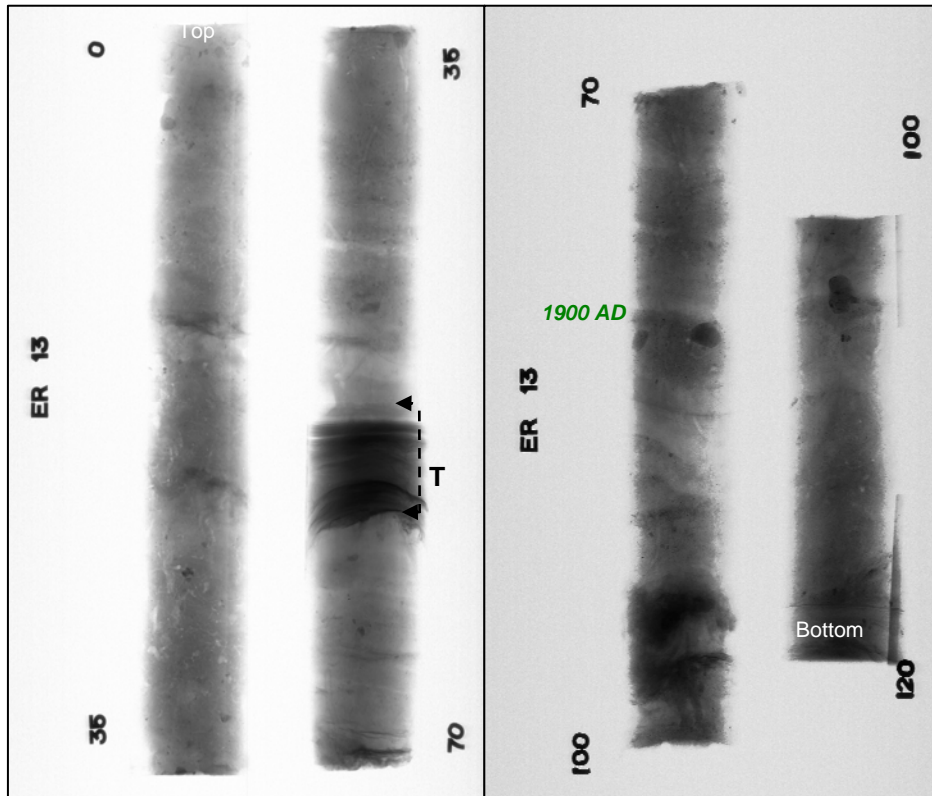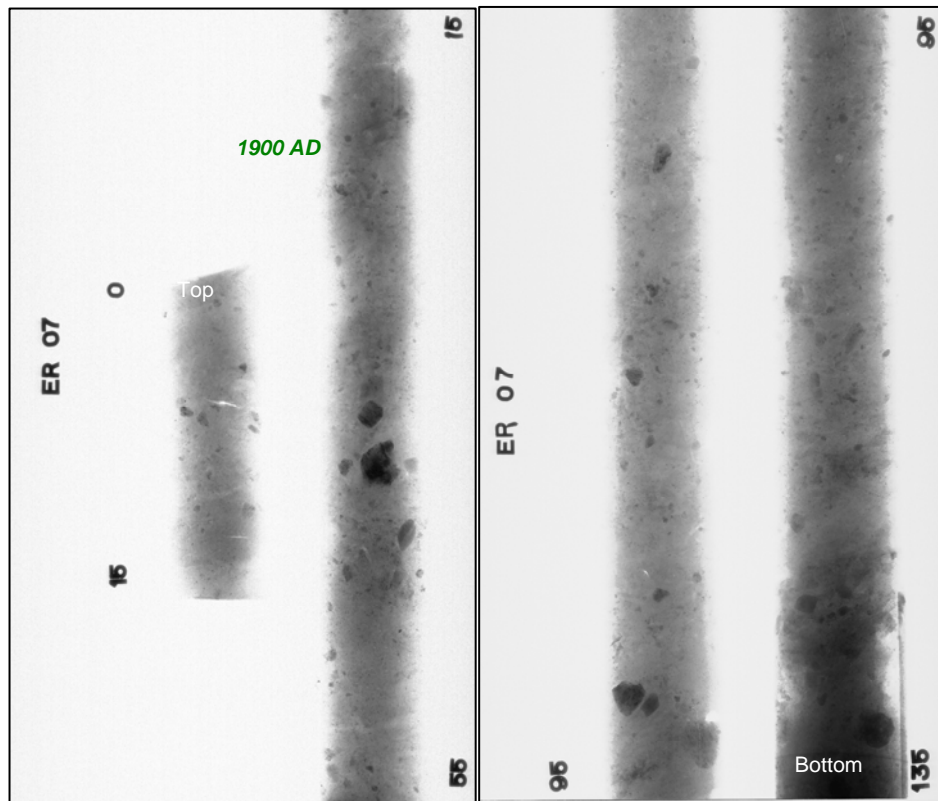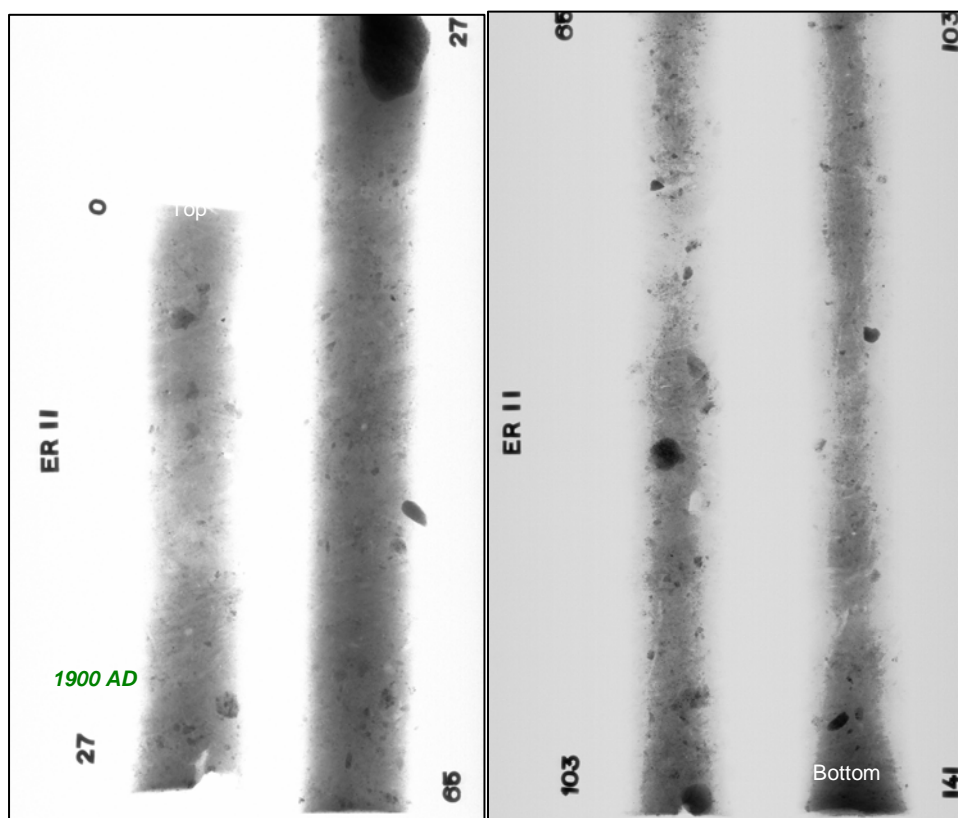
ER11

Supplementary Figure 1. X-ray radiography of cores ER13 (T indicate turbidite), ER07 and ER11. The depth in the core dated to 1900 AD is indicated.

2.2 ^{210}Pb dating and age models

The chronology was established by measuring the ^{210}Pb and ^{137}Cs activity at the Gamma Dating Centre, Department of Geography and Geology, University of Copenhagen (Supplementary Fig. S2). The samples were analysed for the activity of ^{210}Pb, ^{226}Ra and ^{137}Cs by way of gamma-spectrometry using Canberra low-background Ge-detectors. ^{210}Pb was measured by way of its gamma-peak at 46.5 keV, ^{226}Ra by way of the granddaughter ^{214}Pb (peaks at 295 and 352 keV) and ^{137}Cs by way of its peak at 661 keV. The age models are based on samples from 31 levels in ER13, 11 levels in ER07 and 9 levels in ER11 (between 5-15 g dry material from 1 cm thick levels). The chronologies were calculated using the CRS-model (Constant Rate of Supply[33]) but calculations of the activities of unsupported ^{210}Pb in the lower part of the cores were based on regression of activity versus accumulated mass depth in order to increase the robustness of the age models. A turbidite in core ER13, characterised by a sudden marked decrease in ^{210}P activity, was omitted in calculation of the chronology. The chronology below the turbidite was calculated using the CIC-model (Constant Initial Concentration[34]) and assuming a constant accumulation rate similar to the average rate above the turbidite. The ^{137}Cs content of core ER13 showed a distinct peak related to atmospheric bomb test maximum in 1963 at a depth of 28 cm (Supplementary Fig. S2). This level was correctly dated to 1963 using the ^{210}Pb data, indicating that the chronology is reliable.

Mass accumulation rates (MAR (kg m^{-2} yr^{-1})) in the cores are estimated as a function of the sediment accumulation rate (SAR (m yr^{-1})) according to ^{210}Pb derived ages (Supplementary Fig. S3) and the dry bulk density (kg m^{-3}). The MAR in core ER13 is three times higher than MAR

3

in ER07 and ER11, and ranges between 4 and 12 kg m^{-2} yr^{-1} (mean kg m^{-2} yr^{-1} 5.9) and documents shorter-term variability, whereas the MAR in the lower-resolution cores ER07 and ER11 ranges between 1 and 3.5 kg m^{-2} yr^{-1} (means 2.5 and 1.7 kg m^{-2} yr^{-1}, respectively) and documents longer-term variability. The mean MARs derived from Sermilik Fjord sediment cores obtained at 40-60 km from the glacier margin are compared with mean MARs derived from sediment cores from two East Greenland fjords, Kangerdlugssuaq and Nansen, that are located 400-500 km further north along the coast and also receive the majority of their sediment load from iceberg rafting[36]. In Kangerdlugssuaq fjord the mean MAR derived from sediments obtained at 50 km from Kangerdlugssuaq Glacier margin is 4.3 kg m^{-2} yr^{-1} and in Nansen fjords mean MARs are 10 kg m^{-2} yr^{-1} by the head of the fjord and 1.7 kg m^{-2} yr^{-1} at 20 km from. Thus MAR varies more along-fjord than between fjords, which likely reflects the dominant but down-fjord diminishing influence from the turbid melt water plume.
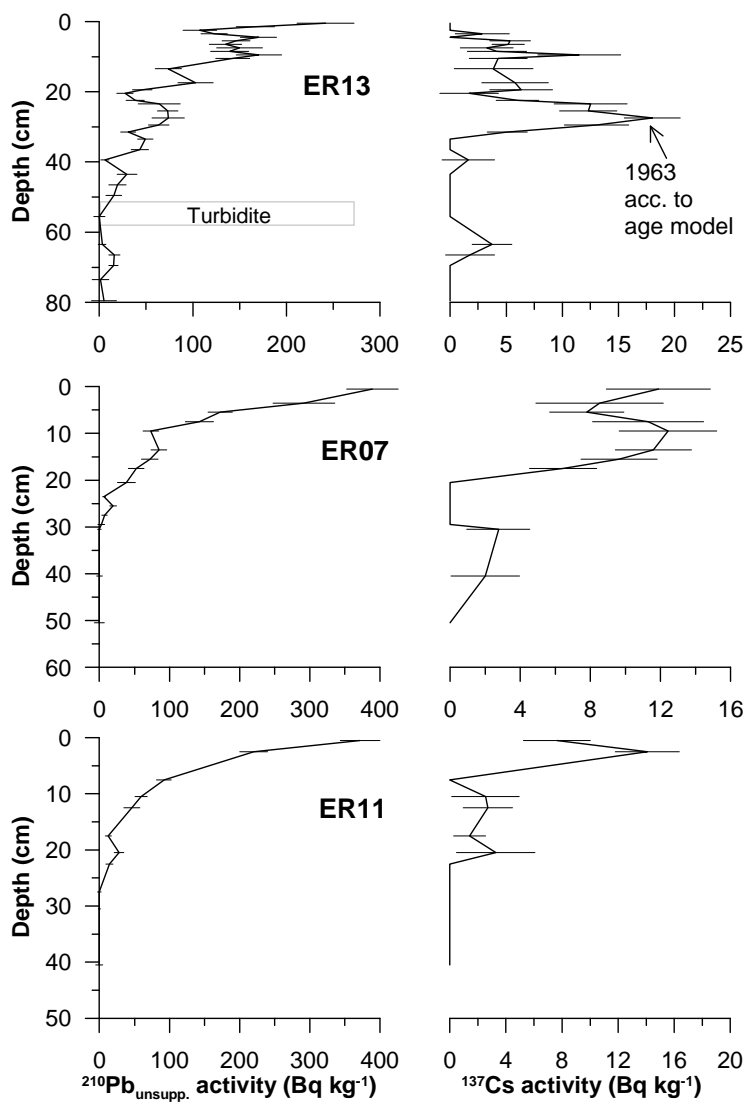
Supplementary Figure 2. ^{210}PB and ^{137}Cs activities as a function of depth (1 sigma error bars).

2.3 Grain size analysis

Grain size distribution (volumen%) was estimated by a Malvern Mastersizer 2000 laser particle sizer at the Skalling Laboratoriet, Department of Geography and Geology, University of Copenhagen. Samples were dispersed with natriumpyrophosphate (0.01 M $Na_4P_2O_7 \cdot 10\ H_2O$) and treated in an ultrasound bath for two minutes before measuring the 0.3-1000 μm fraction. Material (c. 4-6 g) was continuously sampled at ½ cm intervals down to 8 cm and at 1 cm intervals from 8 to 80 cm in core ER13. In core ER07 and core ER11 material was continuously sampled at intervals of ½ cm down 26 cm and 25 cm, respectively. The cumulative volume percentage was determined for the clay and silt fraction (<63 μm) and the sand fraction (63-1000 μm). Core ER13 contains between 0-25 % sand (mean 9 %) in the 63-1000 μm fraction, the content of silt is around 48-65 (mean 52 %) and the content of clay is around 30-45 % (mean 37 %) (Supplementary Fig. S3c). The turbidite at 51.5-58 cm (Supplementary Fig. S1 and Fig. S3c) consists of 72 % sand. The turbidite was omitted from the dataset. The X-ray radiography indicates homogenous deposition during the last 100 years, but grain size measurements reveal variability on decadal timescale. Core ER 07 contains 10-30 % sand (mean 22 %) in the 63-1000 μm fraction, the content of silt is around 40-50 % (mean 45 %) and the content of clay is around 30-42 % (mean 37 %) (Supplementary Fig. S3b). Core ER 11 contains 16-22 % sand (mean 18 %) in the 63-1000 μm fraction, the content of silt is around 44-52 % (mean 49 %) and the content of clay is around 30-40 % (mean 35 %) (Supplementary Fig. S3a).

5
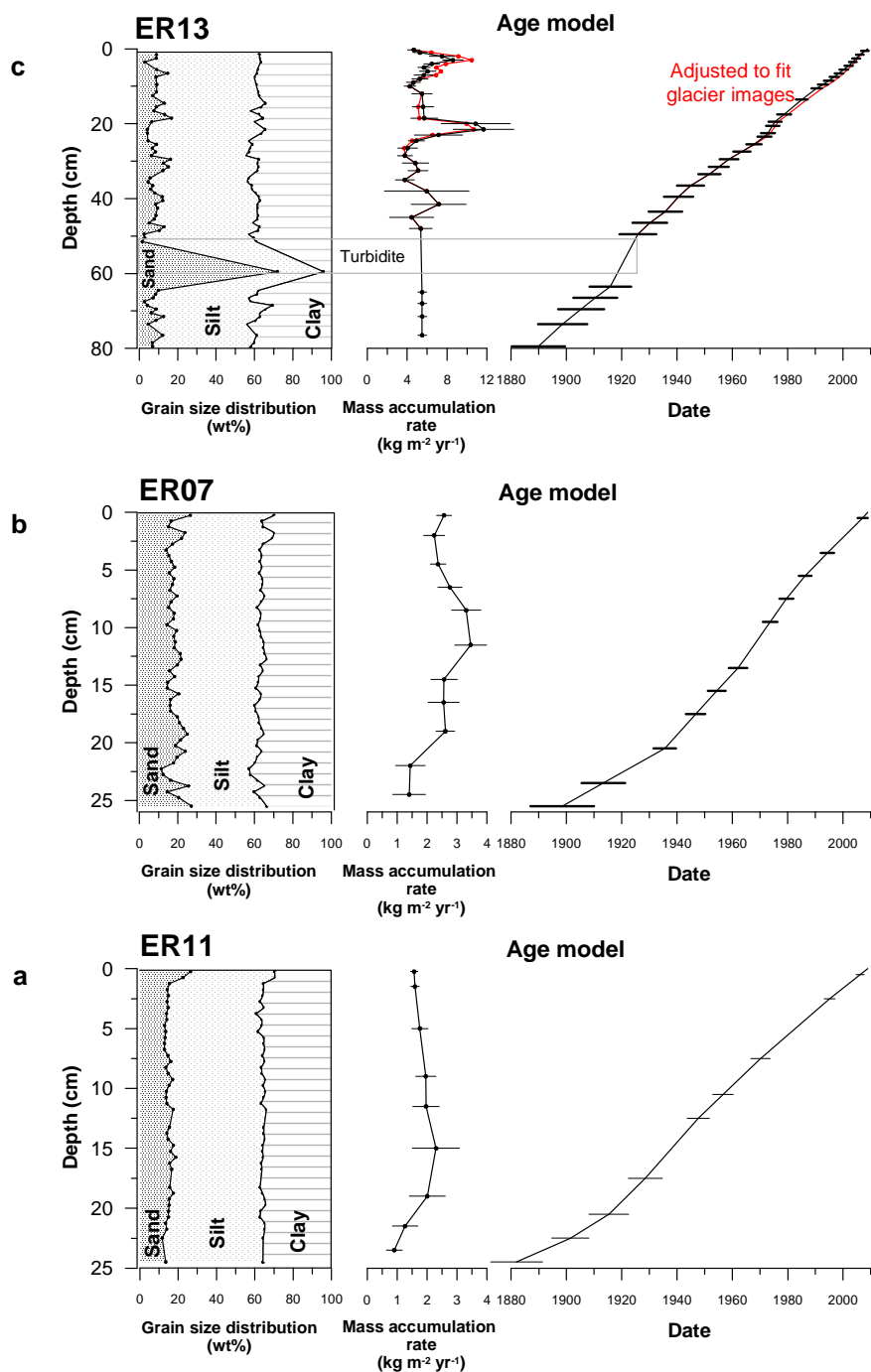
Supplementary Figure 3. Grain size distribution (%) and mass accumulation rate according to ^{210}Pb dating as a function of depth and age-depth models (1 sigma error bars). a. Core ER11. b. Core ER07. c. Core ER13. The red line indicates the fitting of peaks in sand deposition rates with glacier images during the interval 1980-2000 and show that the fit is within the 1 sigma error bar of the age model.

2.4 Sediment deposition and calculation of the composite sand rafting record

The main sources of sediment are: 1) clay and silt suspended in the melt water plume and 2) clay, silt and sand from iceberg rafting (IRD) (Supplementary Fig. S4). Clay and silt from IRD is contributed to all three cores, whereas clay and silt from melt water plume suspended sediment is

6

primarily contributed to ER13 and to a much lesser extent to ER07 and ER11 explaining the higher sedimentation rate in ER13 (Supplementary Fig. S3). This is also verified by oceanographic observations[13] documenting that the amount of particulate matter suspended in sea water is negligible at the ER07 and ER11 core sites.
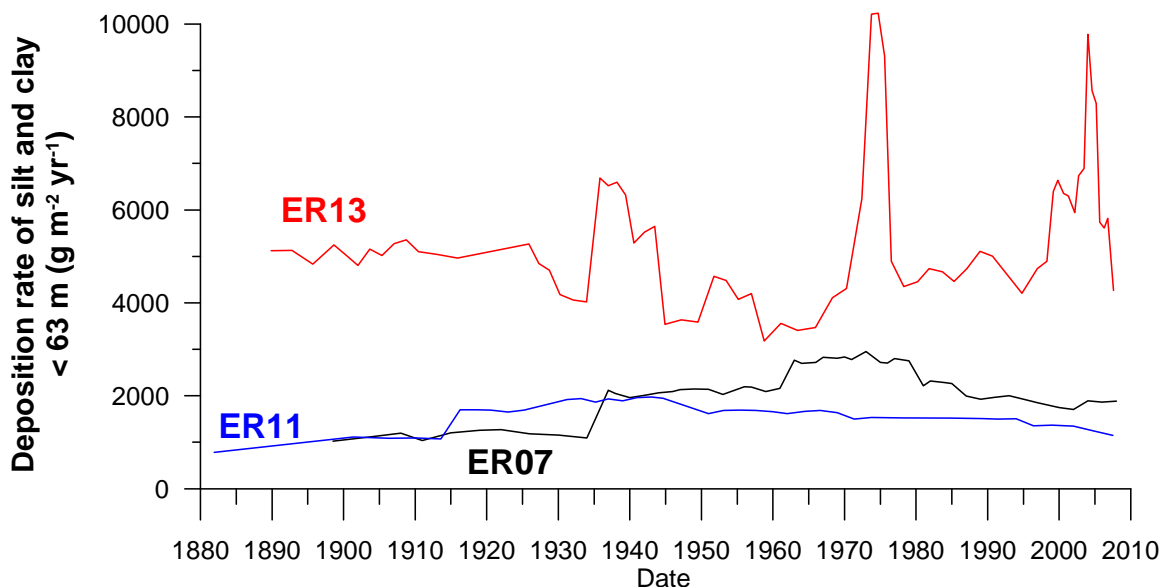
Supplementary Figure 4. Flux of clay and silt. Calculated as a function of silt and clay content (%) and mass accumulation rate (MAR) according to age models. For core ER13 the adjusted age model in Supplementary Fig. S3c is used.

Sand deposition rates in the three cores were estimated as the flux of sand grains (g m^{-2} yr^{-1}), calculated by multiplying the MAR with the content of sand (%) in the respective level. The error (1 sigma) of the sand deposition rate is estimated as the error (1 sigma) of the MAR multiplied by the content of sand (%). The with mean sand flux values is 510 g m^{-2} yr^{-1} in ER13, 481 g m^{-2} yr^{-1} in ER07 and 281 g m^{-2} yr^{-1} in ER11.

The sand deposition rate in the most ice proximal core ER13, shows intra-decadal variability in sand deposition rates compared to the mostly multi-decadal variability in ER07 and ER11 (Fig. 2 in paper). This is explained by the high melt water plume sediment deposition rate in ER13, which allows a higher sampling resolution (mean 1.8 yrs pr 1 cm thick sample) in contrast to the more distal cores ER07 and ER11, where a more condensed stratigraphy results in a relatively smaller sampling resolution (means of 2.2 and 3.1 yrs pr ½ cm thick sample, respectively). The down-fjord decrease in sedimentation rate also increase the influence from sediment mixing by its smoothing of the high-frequent variability.

The composite sand deposition rate was produced as an average of the sand deposition rate in all three cores. In years where only one or two of the cores where presented by a value, the core with a missing value was interpolated. However, there are two exceptions when an interpolation of data in the individual cores became questionable: 1) In the period 1916-1926 (with no data in core ER13), here the composite record is an average of only ER11 and ER07 as sand deposition rates in ER13 may be unstable (see Fig. 2c in paper. 2) In the time period 1890-1899 (the oldest value of ER07 is 1899), here the composite is an average of only ER13 and ER11. We find it plausible to interpolate ER11 in the period 1880-1900 as the data suggest stable sand sedimentation

7

rates (Fig. 2 in paper). The number of values before interpolation is 42 in ER11, 51 in ER07 and 65 in ER13. After interpolation the number of values in the composite record is 98.

The input of sand from Midgaard and Fenris Glaciers is expected to be minimal as these glaciers contribute only a fraction (according to model estimates maximum 25%[14]) of the discharge from Helheim Glacier and furthermore only are expected to influence the mid-fjord core sites ER07 and ER11. Altogether it is expected that they contribute <14% to the composite and that they are not influential on the high frequency variability as this is mostly inherited from core ER13.

It has been considered whether the fjord and shelf IRD deposition rates may be influenced by a relatively long residence time of icebergs (several years[37]) in the sikkusaq in front of the glaciers, whereby potentially relative large amounts of sediment can deposit out[15,38]. The present residence time in the mélange in front of Helheim Glacier is, however, short (on the order of weeks in summer time) and generally far less than a year (pers. comm. Kilian Scharrer, University of Swansea and Gordon Hamilton, University of Maine). It is possible that this have been slightly different in the past 120 years, but given the dynamic nature of the fjord that is observed[11,12] and the strong wind events in this region of Greenland (katabatic and barrier wind events) it is unlikely that the residence time would have been dramatically different. It is thus assumed that variability in the residence time does not influence significantly on the variability of sediment content in icebergs, and thereby the variability in the IRD deposition in the fjord over the investigated time span of this study; i.e. the IRD variability is controlled by the *number* of icebergs exiting the mélange and not the variability in the iceberg sediment load.

3. Helheim Glacier margin images

For documentation of past glacier margin positions, images from satellite and aerial photographs were geo-referenced using ortho-rectified aerial photographs from 1981 with a 2 m spatial resolution (Supplementary Fig. S4). All images represent the glacier margin position late in the melt-season with the majority of the images taken between late August and early September. The latest image in the melt season was chosen during years with multiple images available. In these cases, only images reflecting the general annual trend were used. The frontal position of Helheim Glacier was drawn, and the distance from the front to a fixed point measured. As the Helheim front is relatively uneven, measuring lines at 500 m equidistance were drawn parallel to the fjord. Resulting glacier length has been calculated as the average of the measured distances. The aerial photograph and satellite images document variability in glacier margin position of at least 8 km since 1933 (Supplementary Figure 4). According to these images maximum retreat of the glacier occurred during 2005, following maximum advance during 1993. However, it is noted that the glacier may have, on occasion, previously reached beyond both positions. Overall, from 1933 to 1972 the front advanced close to its maximum position. During the period 1979-2001 the images document retreat and advance of the front within a zone extending 4 km west from the maximum position. From 2002 onwards the front experienced a number of rapid and major retreats with subsequent readvances after 2005 within a zone extending 5 km east of the minimum position.

A comparison between the glacier images and the reconstructed calving record (Fig. 3d in paper) show increased sand deposition concurrent with the retreat of glacier margin positions, including the 2001-2005 thinning, acceleration and retreat of Helheim Glacier and the 1987 and 1979 relatively minor glacier margin retreats. This similarity has been improved by adjusting the chronology of ER13 towards a timescale two years older (which is within 1 sigma error bar of the age model see Supplementary Fig. S3c) in the interval 1980-2000. The correlation coefficient is 0.36 and statistically significant (at the 95% level).

8
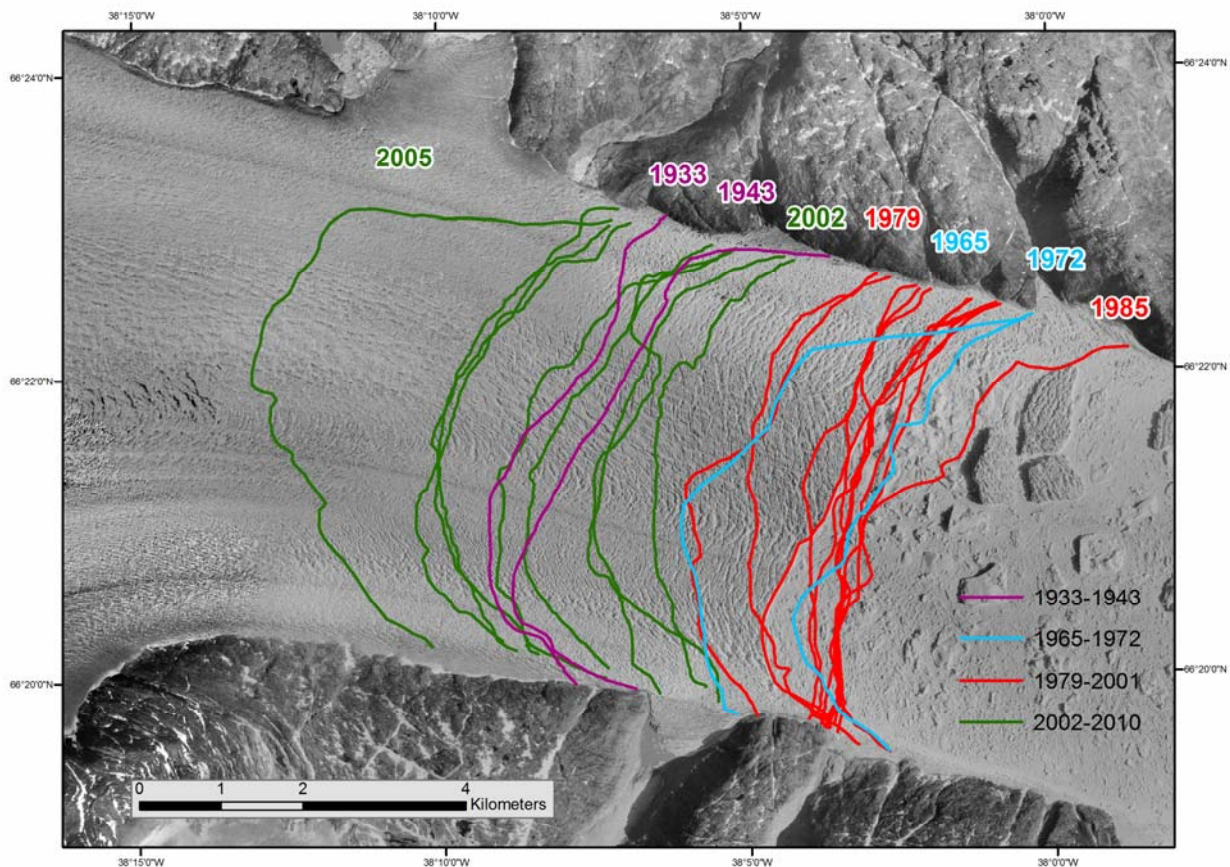
Supplementary Figure 5. Frontal variation in Helheim Glacier margin position from 1933 to 2010 grouped into time frames characterised by similar frontal behaviour. Background image: 1981 ortho-rectified vertical aerial photograph. Data from oblique (1933) and vertical aerial photographs (1943, 1981). Satellite images from Corona-satellite (1965), Landsat 1 (1972), Landsat 4-5 MSS (1986, 1986, 1992), Landsat 7 TM SLC-on (1999-2002), Landsat 7 TM SLC-off (2003-2010) and SPOT (1987-1991, 1993-1996).

4. Oceanographic data

4.1 SST measurements south of Iceland as a proxy for AW variability

The Atlantic Water in Sermilik Fjord is contributed from the Irminger Current which flows along Greenland's southeast and western continental shelf as a western component of the North Atlantic Current. Upstream of Greenland, these waters occupy a layer of several hundred meters which extends to the surface – and periods of increased Atlantic Water (AW) temperature are also associated with a thickening of the AW layer[35]. Thus sea surface temperature (SST) of the AW in a region upstream of Sermilik Fjord is used as a proxy for the variability in the volume and temperature of the Atlantic Water found just offshore of the fjord. The source AW time series was constructed using annual mean surface temperature (and salinity) for an area south of Iceland (20−30° W, 60−63° N) for the period 1876-2007 (salinity from 1945). Surface data were obtained from the ICES (International Council for the Exploration of the Sea) database (www.ices.dk) and monthly mean anomalies were calculated. Annual means were constructed using the monthly

9

anomalies and finally the average temperature and salinity were added to convert anomalies to annual means. The time series extends back to 1921 for temperature and 1945 for salinity. The time series for temperature was then extended back to 1876 using a surface temperature climatology initiated from 1876[39], and maintained until 1975[40] (following termed Smed's series). Smed used data available within the same region south of Iceland (Area F[40]) to estimate monthly means. The overlapping period shows that the temperature data from Smed's time series is consistent with our calculated annual mean temperature based on the ICES data. The correlation coefficient is significant with r=0.79 for the de-trended overlapping period. The difference between the ICES and Smed's series for the overlapping period is 0.13°C, which was subtracted from the full Smed series. Given the high similarity of the time series, following, a mean of the values of Smed and ICES data were used for the overlapping period. Finally, to convert the anomalies to "real" temperatures, +9.00°C was added to the series; this corresponds to the offset between the monthly mean ICES anomaly relative to the monthly mean raw ICES's series for the overlapping period 1921−1975. The correlation coefficient (r-value) between salinity and temperature is 0.59 (statistical significant at the 99.5% confidence level) illustrating that temperature changes are related to changes in the water masses of the subpolar gyre and not only to atmospheric warming in the region south of Iceland.

The constructed time series compared favourably with an observational dataset (covering the time period 1970-2009) of subsurface water temperatures (0-200 m) obtained from the southern shelf of Iceland (Selvogsbanki Station 5)[41] supporting the notion that the variability in SST from our chosen region is a reliable approximation of the variability of subsurface waters.

4.2 Multiyear sea-ice (Storis) extent as a proxy for Polar Water variability
The amount of multi-year sea ice (Storis) that exits The Arctic Ocean via Fram Strait, around Cape Farewell and onto the SW Greenland shelf is used as a proxy for the variability in the Polar Water volume flowing out of Fram Strait and around Greenland. A long time series of the northernmost Storis extent along southwest Greenland in May, June and July covering the period 1820-2000[25] was used and furthermore updated to 2010. The Storis Index has been defined[42] as the northernmost position on the southwest coast, relative to Cape Farewell, of Storis exported through Fram Strait based on ice charts made at the Danish Meteorological Institute. It was an extension and modification of a similar index[43] and gives the monthly values for the period 1900−1972. Later the time series was extended back to 1820[44] using the method by Speerschneider[45]. Our update 2000-2010 is based on analysis of 3-7 images per week.

Storis usually transits Cape Farewell around Christmas time, though the exact time can vary by several months from year to year. The largest extent usually occurs in late spring/early summer. This fortunately coincides with the months (May, June, July) with the most complete data coverage above 90%. The series of Storis extent for these months were standardized by removing the long-term average and dividing by the long-term standard deviation. The average of the three standardized months was defined as the summer Storis-index.

A significant cross-correlation with a lag of 0 and 1 year has been found between the Storis Index and the volume transport of sea-ice through Fram Strait derived from an ocean model[25]. A long time series of sea-ice transport through Fram Strait was constructed using a linear combination of the Storis Index for a specific year and the former year[25]. As Sermilik Fjord is found downstream of Fram Strait but closer to Cape Farewell, we used the un-lagged Storis Index and assumed that the Index is representative of the Storis transport on the shelf outside Sermilik Fjord in early wintertime – corresponding to a lag of almost half a year. Next, it is assmued that the Storis Index is a proxy for the Polar Water transport within the East Greenland Current. This assumption is supported by the notion that episodes of anomalous fresh water discharge from the Arctic Ocean,

known as Great Salinity anomalies (GSAs), which occurred in the 1970s, 1980s and 1990s[30], are all clearly represented in the Storis Index.

4.3 Shelf Index

The East Greenland shelf waters which are replenished with Sermilik Fjord are characterized by an upper layer of cold, fresh Polar Water (PW) and a deeper, subsurface layer of Atlantic Water (AW)[46]. The relative partitioning of these water masses changes both seasonally[12] and inter-annually (as shown by changes in SST on the shelf[9]). While the precise mechanisms driving such changes are presently unclear, they are likely tied both to changes in the subpolar gyre circulation offshore and to changes in the transport of the East Greenland Current carrying PW on the shelf. For example, the slow down of the subpolar gyre since the mid 1990s[47] has been associated with an increase in the temperature and volume of the AW in the subpolar region[48] and a warming of the bottom waters on the West Greenland shelf[8], suggesting that the volume of AW on the Southeast Greenland shelf also increased during this period. Similarly, increased fresh water export from the Arctic results in freshwater anomalies (Great Salinity Anomalies[30]) that travel around the Greenland shelf and progressively mix into the subpolar gyre's interior[29]. Thus, this suggests that the East Greenland shelf is influenced both the Atlantic and Arctic variability.

Given this, and the lack of long term measurements from the East Greenland shelf, we construct a Shelf Index in order to account for the combined variability of the AW and PW. To do this, the proxy records for the AW source and PW (the Storis Index) are normalised (by subtracting the mean and dividing by the standard deviation) and a Shelf Index is constructed by subtracting the resultant PW index from the AW index (Supplementary Fig. S6). In this way the two water masses are weighted 1:1 in the Shelf Index – which seems legitimate since there is not enough information implying a more specific weighting of either water mass. A positive (negative) Shelf Index implies increased (decreased) influence of AW and decreased (increased) influence from PW on the shelf. The validity of the proposed Shelf Index is tested via comparison with two independent data-based temperature records; one from the nearby Irminger Sea interior and one from the SW Greenland shelf. The general idea is that a warmer SST in these regions will be associated with an increased volume of AW on the shelf. The Irminger Sea interior is chosen preferentially over the shelf since measurements on the shelf are scarce and subject to large uncertainties due to the simultaneous presence of both PW and AW. Lateral mixing between the shelf and the interior of the Irminger Sea, however, tends to transmit the lower-fequency (seasonal, inter-annual) shelf variability to the gyre interior. Thus, the upper ocean properties of the basin interior are likely to capture the variability on the shelf. This direct connection between the shelf and the interior is manifested in the more studied Labrador Sea, for example, where the fresh anomaly transiting around the shelf in the late 1960s simultaneously drove a cooling and freshening of the upper layers of the gyre interior[29]. Here, we use SST from the Irminger Sea interior, defined as the region offshore of the 2500m isobath, and extracted from the HadISST[43] as an independent indicator of the shelf variability to compare with the Shelf Index.

A second observational data used for validation of the Shelf Index are the repeat hydrographic surveys collected at Fylla Bank off Southwest Greenland which exist for the period 1876–2010[50]. While these measurements are on the southwestern side of Greenland, the continuity of the East and West Greenland Currents around Cape Farewell suggests that the variability at Fylla is also representative of that along the upstream, southeast Greenland shelf.

A good correspondence is found between the Shelf Index and both datasets with statistical significant (99.5%) correlation coefficients of 0.65 (with HadISST) and 0.39 (with Fylla Bank temperature data), supporting the notion that the Shelf Index adequately represents the combined PW/AW variability on the East Greenland shelf.

11
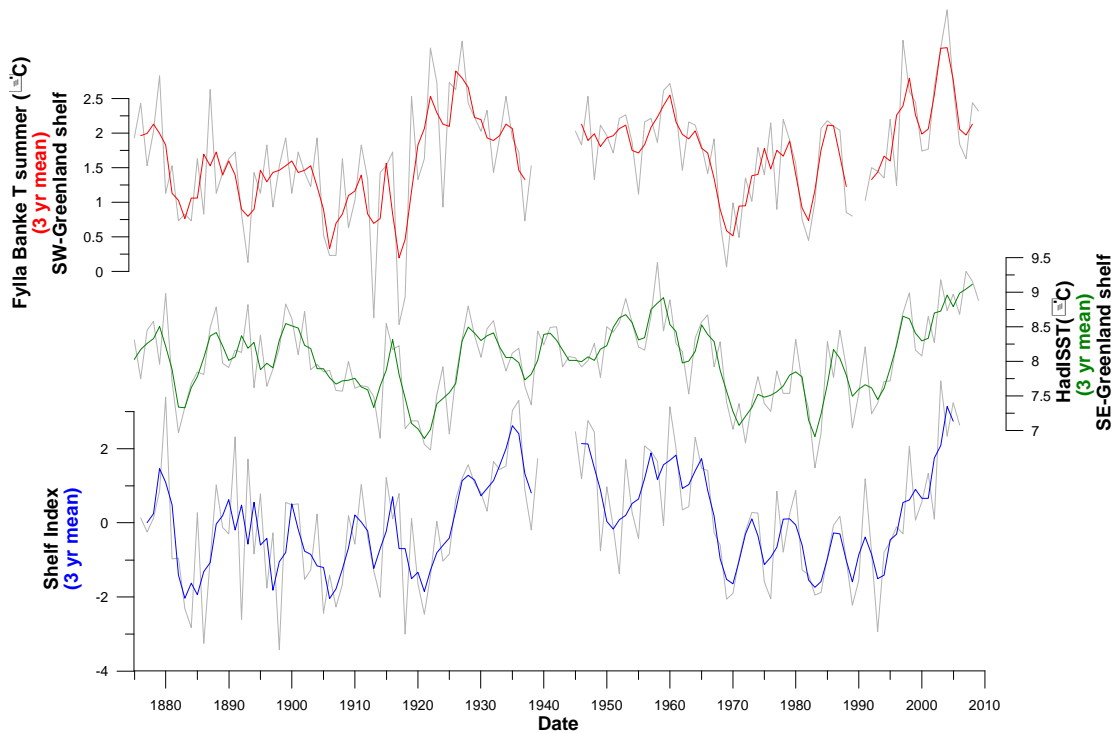
Supplementary Figure 6. Shelf mix Index, HadISST[49] T$_{summer}$ (°C) from the Irminger Basin and mid-June temperature on top of Fylla Bank (0-40 m)[50].

5. Statistical computations

In order to test the correlation between the climate indices and the calving record a series of statistical computations were carried out. All data except the calving record were filtered with a 3 year running mean. This was done in order to compensate for uncertainties in the age model of the calving record in the calculation of correlation coefficients. Then all data were linearly detrended and the final dataset is termed the *bulk dataset* (Supplementary Fig. S7). In order to differentiate between multi-decadal variability and shorter (decadal to inter-annual) variability the data were low-pass filtered with a 25 year Fourier filter which removes the short-term variability and highlights the longer-term (multi-decadal) variability. The Fourier filter was chosen preferably to other filters because it allowed us to preserve more data at the end points of the data sets. To evaluate the short-term variability the residuals were estimated by subtracting the filtered data from the bulk data set.

12
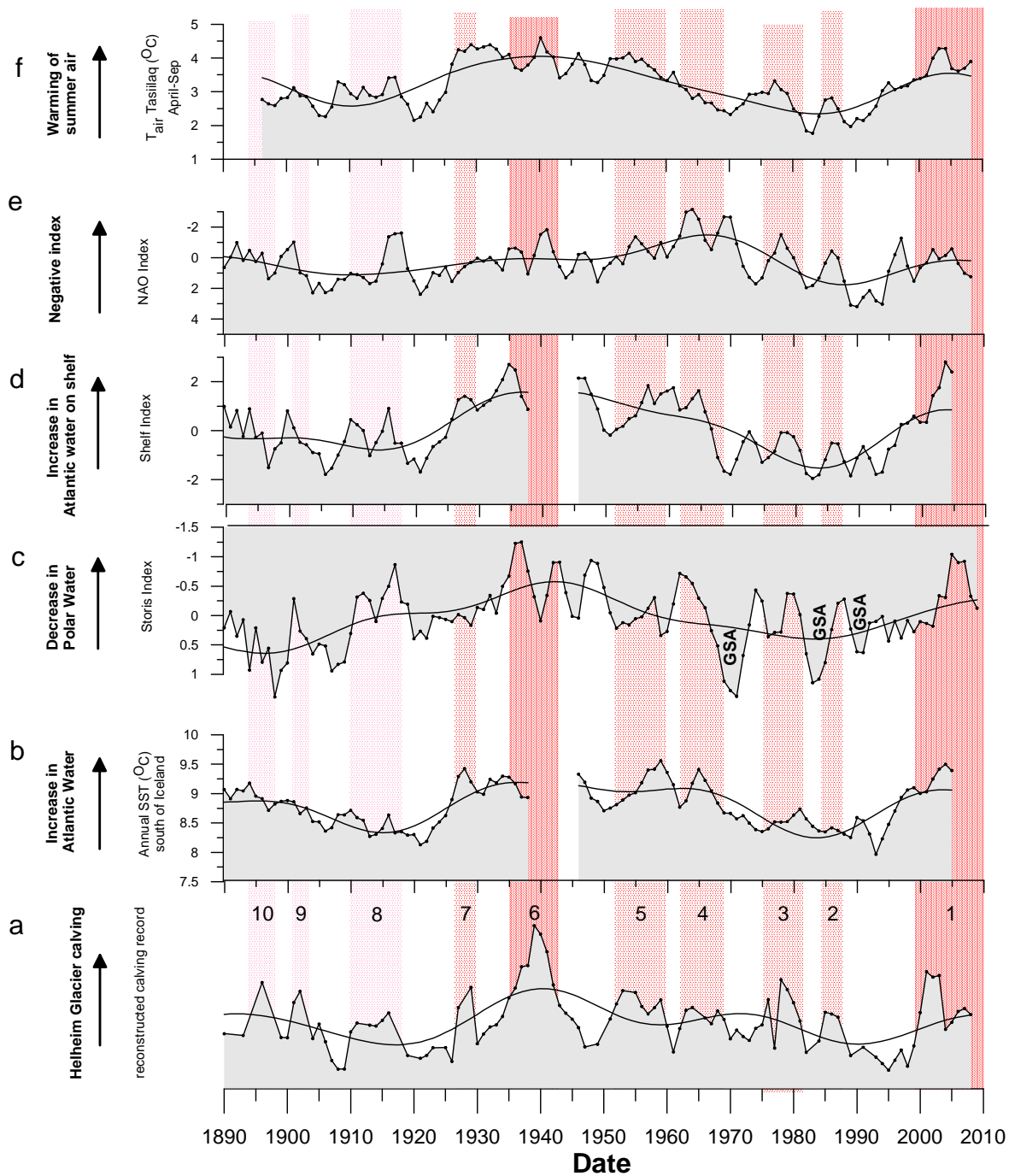
Supplementary Figure 7. Data filtered using a 3 year running mean (except the calving record) and linearly detrended. The 25 year low-pass filter is overlaid on each time series.

Pearson correlation coefficients were calculated between the calving and the climate data for bulk data, the low pass filtered data and the residuals (after linearly detrending the data sets). For the calving data (N-2=96) r values≥ 0.17 are statistically significant at the 95% level of confidence. For the 3 year filtered climate data (N-2=96/3) r values ≥ 0.288 are statistically significant at the 95% level of confidence. Thus, when calculating correlation coefficients between calving and climate data (bulk and residuals) the definition of r-values ≥ 0.29 as statistically significant (95% level of confidence) is a conservative estimate. When calculating correlation

13

coefficients between the Fourier-filtered data (N-2=96/25), the statistically significant r-values increase to 0.74 (95% level of confidence). Both the AW and the derived Shelf Index have a gap from 1940 to 1945, while the calving record has 3 values in that period, which further reduces the degrees of freedom (N-2=93). For bulk and residual correlation coefficients this means that r values ≥ 0.292 are statistically significant at the 95% level of confidence and for correlation of Fourier-filters (N-2=93/25) r values ≥ 0.75 are statistically significant at the 95% level of confidence.

The bulk correlation coefficients (Table 1 in paper) show significant correlation between calving and all of the investigated climate indices for the bulk datasets. The correlation coefficients between the low-pass filtered datasets indicate a correlation between calving and AW temperature and summer air temperature, which would likely improve by wiggle matching the calving record with the two climate records. Considering the minor age uncertainties of the calving record we find it plausible to conclude that the multi-decadal variability in calving is correlated with changes in the AW and air temperature – which, in turn, are highly correlated on these time scales (correlation coefficient of 0.88). The correlation between calving and Shelf Index on multi-decadal timescales mainly reflects the multi-decadal variations in AW temperature.

By calculating the correlation coefficients between the residual data sets of the calving and the climate data a statistically significant correlation is found between short-term calving episodes, a negative NAO index and a positive Shelf Index. The correlation with short-term warming of the AW is 0.27 and close to the r-value of 0.29 for a statistical significant correlation at the 95% level of confidence. The correlation coefficient between the residuals of the NAO index and the residuals of the Shelf mix Index is -0.41 which is statistically significant at the 99.5% level of confidence.

The statistical analysis conducted above is supported by constructing a composite of the ten episodes with the highest calving activity on the record (HC1-HC10, Supplementary Fig. S7) and one for the ten lowest calving episodes (LC1-LC9) as identified from the residuals in the calving record. The mean values of the residual climate proxies are then calculated for both the high and low calving composites. The composite analysis supports that a high calving activity is associated with significant positive anomalies in the Shelf Index, the summer air temperature, the AW and a negative NAO phase. On the other hand, reduced calving activity is associated with a significantly large PW (increased sea-ice flux) and a positive NAO Index, suggesting that a thicker, colder PW layer can reduce calving activity on short time scales. The fact that the ratio between mean and standard deviation is highest for the Shelf Index suggests that changes in calving are mainly driven by the relative influence of AW and PW.

Calving episodes	Calving	T_{air} summer	NAO index	Sea ice flux	Atl. Water T_{annual}	Shelf Index
Mean+/-stdv of mean (HC)	58+/-7.5	0.21+/-0.11	-0.36+/-0.15	-0.05+/-0.07	0.11+/-0.04	0.43+/-0.09
Mean+/-stdv of mean (LC)	-48+/-3.9	-0.05+/-0.1	0.39+/-0.12	0.3+/-0.09	-0.05+/-0.04	-0.16+/-0.16

Supplementary Table 1: Mean values of residuals (+/- standard deviation of the mean) during an average high (HC) and an average low (LC) calving episode.

References for supplementary information

31. Schjøth, F. and Andresen, C.S. From unknown sea bed morphology in the Sermilik Fjord, Southeast Greenland to a bathymetric map based on more than 500.000 echo sounder and Chirp sub-bottom profiler measurements (abstract & poster). *ESRI Europe, Middle East and Africa User Conference, 26 - 28 October 2010, ESRI Italia, Rome, Italy* (2010).

32. Andresen, C.S., Nørgaard-Pedersen, N., Jensen, J. B., and Larsen, B. Southeast Greenland ice-sheet variability elucidated by shallow seismic survey and sediment coring in the Sermilik Fjord near the Helheim Glacier in 2009. *Geological Survey of Denmark and Greenland Bulletin 20*, 83-86 (2010).

33. Appleby, P. G. and Oldfield, F. The assessment of ^{210}Pb data from sites with varying sediment accumulation rates. *Hydrobiologia 103*, 29-35 (1983).

34. Appleby, P.G. Chronostratigraphic techniques in recent sediments. In: Last, W.M & Smol, J.P. (eds) Tracking environmental change using lake sediments. *Volume 1: Basin analysis, coring and chronological techniques*. Kluwer Academic Publishers, the Netherlands (2001).

35. Våge, K. et al. The Irminger Gyre: Circulation, convection, and interannual variability. *Deep Sea Research Part I: Oceanographic Research Papers 58(5)*, 590–614 (2011).

36. Smith, L. M., Clark, A. and Jennings, A. E. Accumulation in East Greenland Fjords and on the continental shelves adjacent to the Denmark Strait over the last century based on ^{210}Pb geochronology. *Arctic 55*, 109-122 (2002).

37. Dwyer, J. L. Mapping tide-water glacier dynamics in East Greenland using Landsat data. *Journal of Glaciology 41*, 584-596 (1995).

38. Andrews, J. T. Icebergs and Iceberg Rafted Detritus (IRD) in the North Atlantic: Facts and Assumptions. *Oceanography 13*, 100-108 (2000).

39. Ryder, C. Monthly mean temperatures of the surface water in the Atlantic north of 50° n.lat. *Appendix to the Nautical Meteorological Annual of the Danish Meteorological Institute* (1917).

40. Smed, J. Fluctuations in the temperature of the surface water in the areas of the northern North Atlantic, 1876−1975. In: *Danish Meteorological Institute Climatological Papers* **4**, 205−210 (1978).

41. Hughes, S. L., Holliday, N. P., and Beszczynska-Möller, A. (Eds). ICES Report on Ocean Climate 2009. *ICES Cooperative Research Report* **304,** 67 pp. (2010).

42. Valeur, H.H.. Polar ice variations off the Greenland west coast 1900–72. *Int. Commission for the Northwest Atlantic Fisheries*, Special Publication **9**, 27 pp. (1976).

43. Fabricius, J.S., and Thomsen, H. Isforholdene ved Grønland (Ice conditions around Greenland). Appendix 29 in *Betænkning* **227**, 126−132. Statens Tryknings Kontor, Copenhagen, Denmark (1959).

44. Fabricius, J.F., Frydendahl, K., and Frich, P. Polar sea ice off West Greenland—A review. Proc. 14th Int. Offshore Mechanics and Arctic Engineering Conf., Copenhagen, Denmark, American Society of Mechanical Engineers, 265–272 (1995).

45. Speerschneider, C.I.H. The state of the ice in Davis Strait 1820–1930. *Danish Meteor. Inst. Medd.* **8**, 1–53 (1931).

46. Sutherland et al. Freshwater composition of the waters off southeast Greenland and their link to the Arctic Ocean. *Journal of Geophysical Research* **114**, C05020, doi:10.1029/2008JC004808 (2009).

47. Hakkinen, S. And P. B. Rhines. Decline of Subpolar North Atlantic Circulation During the 1990s, *Science* **304**, 555-559 (2004).

48. Hatun, H., A. B. Sando, H. Drange, B. Hansen, and H. Valdimarsson. Influence of the Atlantic Subpolar Gyre on the Thermohaline Circulation, *Science* **309**, 1841-1844 (2005).

49. Rayner, N.A., et al. Globally complete analyses of sea surface temperature, sea ice and night marine air temperature, 1871-2000. *J. Geophysical Research* **108**, 4407, doi:10.1029/2002JD002670 (2003).

50. Ribergaard, M.H. Oceanographic Investigations off West Greenland 2010. *NAFO Scientific Council Documents* **11/001** (2011).